

Multidimensional Simulations of the Accretion-induced Collapses of Dark Matter-admixed Rotating White Dwarfs: Dynamics and Gravitational-wave Signals

HO-SANG CHAN ¹, MING-CHUNG CHU ¹ AND SHING-CHI LEUNG ^{2,3}

¹*Department of Physics and Institute of Theoretical Physics, The Chinese University of Hong Kong, Shatin, N.T., Hong Kong*

²*Department of Mathematics and Physics, SUNY Polytechnic Institute, 100 Seymour Road, Utica, New York 13502, USA*

³*TAPIR, Walter Burke Institute for Theoretical Physics, Mailcode 350-17, Caltech, Pasadena, CA 91125, USA*

Submitted to ApJ

ABSTRACT

Despite Dark Matter (DM)-admixed neutron stars have been extensively studied, there is still no in-depth research addressing their formation channel. Here, we present two-dimensional hydrodynamic simulations of the accretion-induced collapse (AIC) of rotating white dwarfs admixed with sub-GeV DM. We find that the DM component would follow the collapse of the normal matter (NM) component to become a bound DM core, with a time scale comparable to that of the NM. Thus, our simulations demonstrate numerically how a DM-admixed neutron star forms through DM-admixed AIC (DMAIC) for the first time. The gravitational-wave (GW) signature from the DMAIC also shows distinctive features. In the diffusive DM limit, the admixture of DM indirectly suppresses the post-bounce spectral peak of the NM GWs for differentially rotating progenitors; In the compact DM limit, the collapse dynamics of the DM generate GWs that are strong enough to directly influence the total GW signature, producing continuous low-frequency (< 1000 Hz) signals in the GW power spectrum after the NM core bounce. We also find that the DM GWs are detectable by the Advanced LIGO, provided that the DMAIC event happens within the Milky-way. We further discover a relationship between the DM mass and its GW peak frequency, and we provide an empirical formula that fits the relation. Not only is our study the first-ever computation of GW from a collapsing DM, but these findings also provide the key features to identify DM in AIC events through future GW detections.

Keywords: Dark matter — White dwarfs — Rotation — Neutron stars — Gravitational Waves

1. INTRODUCTION

1.1. Dark Matter-admixed Astrophysical Objects

Dark Matter (DM) constitutes more than 95 % of the mass in a typical galaxy (Freese 2017) and 23 % of the mass-energy budget of the Universe (Peter 2012). It is natural to hypothesize that stellar objects comprising normal matter (NM) and DM may form. Indeed, DM could be captured by NM in a region with a high concentration of DM particles (Casanellas & Lopes 2009; Sulistiyowati et al. 2014; Arun et al. 2019). Stars may then contain a DM component. There have been extensive theoretical studies on the possible effects of admixing DM to the stellar evolution models (Lopes & Lopes 2019; Clea et al. 2020; Raen et al. 2021). Unusual objects that are consistent with such models might provide hints about the existence of DM-admixed stars. Furthermore, there are studies utilizing DM-admixed star models to constrain the properties of DM. For instance,

Leung et al. (2022) proposed a method for inferring the DM particle mass by measuring the tidal deformability of neutron stars. Bramante et al. (2013) and Bell et al. (2013) constrain the particle mass and annihilation cross section for bosonic DM using the DM-admixed neutron star model. These examples show that DM-admixed stellar objects could be a promising channel to probe astrophysical DM.

1.2. Rotating White Dwarfs

The majority of studies regarding WD assumed it is not rotating. However, observational evidence showed the opposite (Spruit 1998; Kawaler 2004). It was suggested that WDs gain angular momentum through accretion from a companion star (Langer et al. 2003; Yoon & Langer 2004) and mergers between two or more WDs (Gvaramadze et al. 2019; Pshirkov et al. 2020). Therefore, rotation is needed to understand the full picture of WD structures and evolution (Yoon & Langer 2004;

Yoon, S.-C. & Langer, N. 2005). In addition, rotating WDs have been proposed to be progenitors of superluminous thermonuclear supernovae because rotating WDs could support more mass than their traditional Chandrasekhar limit (Pfannes, J. M. M. et al. 2010; Wang et al. 2014; Fink, M. et al. 2018). Recently, theoretical studies have been made on finite-temperature corrections to the modeling of rotating WDs (Boshkayev 2018; Yoshida 2019), as well as effects of the strong magnetic field on the equilibrium structures of WDs (Franz & Schramm 2015; Bera & Bhattacharya 2016; Chatterjee et al. 2017), for which the WD rotation takes a critical role. Including rotational effects would now be essential for state-of-the-art WD modeling.

1.3. Accretion-induced Collapse

It was widely believed that WD would undergo a thermonuclear supernova when its mass is approaching the canonical Chandrasekhar limit. However, it is natural to expect that the electron-degenerate pressure would not be able to support the over-massive WD core, leading to a direct gravitational collapse - AIC. In particular, AIC occurs when the mass of a WD containing an Oxygen-Neon core increases towards the Chandrasekhar limit through stable accretion from a companion object (Nomoto & Kondo 1991; Wang 2018; Ruiter et al. 2019), though a binary WD merger seems to be another possible scenario (Liu & Wang 2020). The collapse is triggered by electron capture in the degenerate matter (Brooks et al. 2017). On the other hand, pycnonuclear burning is also possible in such an extremely dense core. Hence the ultimate fate of an Oxygen-Neon WD would depend on the competition between nuclear runaway and electron capture (Wang & Liu 2020). However, it was later found that the central temperature of Oxygen-Neon WDs is insufficient for explosive oxygen-neon burning (Wu & Wang 2018). Even if deflagration occurs, it fails to unbind the WD, which directly leads to a collapse for a wide range of parameters (Leung & Nomoto 2019; Zha et al. 2019b; Leung et al. 2020).

Besides the iron-core collapse of massive stars, the AIC of WDs has been proposed as another channel for forming neutron stars. However, AIC is much less energetic than typical core-collapse supernovae. The small amount of nickel synthesized indicate that they are usually faint transients (Darbha et al. 2010). On the other hand, AIC emits radio signatures (Moriya 2016) and has been hypothesized as potential candidates for Fast Radio Burst (Margalit et al. 2019) and Millisecond Pulsars (Wang et al. 2022). These examples show that

electromagnetic-wave detection of AIC would be a challenging but possible task. Nonetheless, the collapse dynamics of the compact iron core are expected to produce strong GW signals (Ott et al. 2005; Ott 2009). Hence, searching for AIC would rely on future GW detection. There have been some efforts to predict the GW signature from an AIC. Dessart et al. (2006) simulated 2D AIC with neutrino transport and estimated GW emission from AIC via the Newtonian quadrupole formalism. They concluded that AIC events could be detected by LIGO-class detectors, given that these events occur within the Milky Way. Abdikamalov et al. (2010) found that the GW signals from an AIC show a generic “Type III” shape, though detailed neutrino physics has been omitted.

1.4. Motivations

Although DM-admixed neutron stars have been studied and applied to explain anomalous compact objects, there is still no in-depth research on their formation channel. Even though Leung et al. (2019); Zha et al. (2019a) numerically investigated DMAIC, they assumed the DM component is spherically symmetric and non-moving. As pointed out by Leung et al. (2019), the non-movable DM approximation may break down if the dynamical time scales for DM and NM become comparable, and the dynamical modeling of the DM becomes important. They also point out that there is a moment during the collapse in which the NM has a mass density comparable with that of the DM. Also, Chan et al. (2021) showed that fermionic DM with a sub-GeV particle mass would produce a massive and extended component comparable to that of the NM. In such a scenario, modeling the DM dynamics would be necessary. Therefore, it seems a natural extension to include DM dynamics in our simulations. In this study, we extend the multidimensional simulations by Zha et al. (2019a) to also model the DM component’s dynamical evolution. Our study aims to investigate if DMAIC could make a DM-admixed neutron star when the DM motion is taken into account and to predict the corresponding GW signature to facilitate searching for DM through observing AIC in the future. The structure of the paper is as follows: we present the methodology in Section 2. We then present our simulation results in Section 3. Finally, we conclude our study in Section 4.

2. METHODOLOGY

2.1. Equation of Hydrostatic Equilibrium

We compute DM-admixed rotating WDs (DMRWs) as DM-admixed AIC (DMAIC) progenitors by solving the Newtonian hydrostatic equations, including the cen-

tripetal force:

$$\begin{aligned}\vec{\nabla} P_1 &= -\rho_1 \vec{\nabla} \Phi, \\ \vec{\nabla} P_2 &= -\rho_2 \vec{\nabla} \Phi + [\rho_2 \omega_2(s)^2 s] \hat{s}, \\ \nabla^2 \Phi &= 4\pi G(\rho_1 + \rho_2).\end{aligned}\quad (1)$$

Here, the subscript $i = 1(2)$ denotes the DM (NM) quantities, and ρ , P , ω , and Φ are the density, pressure, angular speed, and gravitational potential of the fluid element. s is the perpendicular distance from the rotation axis, and \hat{s} is the unit vector orthogonal to and pointing away from that axis. The angular speed is assumed to be a function of s only. We consider the Newtonian framework because the rotation speed and compactness of WDs are low.

We follow [Eriguchi & Mueller \(1985\)](#), [Hachisu \(1986\)](#) and [Aksenov & Blinnikov \(1994\)](#) to integrate the equation of equilibrium:

$$\begin{aligned}H_i + \Phi + \delta_{i2} h_i^2 \psi_i &= C_i, \\ \int \frac{dP_i}{\rho_i} &= H_i, \\ \int \omega(s)_i^2 s ds &= -h_i^2 \psi_i.\end{aligned}\quad (2)$$

where C_i is an integration constant, H is the enthalpy, ψ is the rotational potential, and h^2 is a constant to be determined [Hachisu \(1986\)](#). We solve the equilibrium equations for the DM and NM using a two-fluid, self-consistent field method (Chan et al. 2022, submitted).

2.2. Rotation Rules

We have considered rotation profiles for the NM from [Hachisu \(1986\)](#) and [Yoshida \(2019\)](#) including (1) the rigid rotation:

$$\omega(s)_2^2 = \Omega_2^2, \quad (3)$$

and (2) fastly rotating core remnants “Kepler” profile:

$$\omega(s)_2^2 \propto 1/(d^{3/2} + s^{3/2})^2. \quad (4)$$

This rotation profile resembles a rapidly rotating core surrounded by an envelope rotating at its Keplerian limit. Here, d is the rotating core radius.

We integrate the angular velocity to obtain the effective potential of the rotation for the rigid rotation:

$$\psi_2 = s^2/2 \quad (5)$$

The effective potential for the Kepler rule is:

$$\begin{aligned}\psi_2 &= -\frac{1}{9} \left[-\frac{6\sqrt{s}}{s^{\frac{3}{2}} + d^{\frac{3}{2}}} + \frac{1}{d} \ln \left(\frac{(\sqrt{d} + \sqrt{s})^2}{d + s - \sqrt{sd}} \right) \right. \\ &\quad \left. - \frac{2\sqrt{3}}{d} \tan^{-1} \left(\frac{1 - 2\sqrt{s/d}}{\sqrt{3}} \right) \right].\end{aligned}\quad (6)$$

2.3. Hydrodynamic Evolution

We solve the two-dimensional Euler equations assuming axial symmetry:

$$\begin{aligned}\partial_t \rho_i + \nabla \cdot (\alpha \rho_i \vec{v}_i) &= 0, \\ \partial_t (\rho_i \vec{v}_i) + \nabla \cdot [\alpha \rho_i (\vec{v}_i \otimes \vec{v}_i)] + \nabla (\alpha P_i) &= \\ -\alpha (\rho_i - P_i) \nabla \Phi.\end{aligned}\quad (7)$$

For $i = 1$ and 2 . Here, $\alpha = \exp(-\phi/c^2)$ is the lapse function with c being the speed of light. It is used to mimic general relativistic time-dilation effects and has been applied to study first-order quantum chromodynamics phase transition in core-collapse supernovae ([Zha et al. 2020](#)). We also solve the advection equation for the NM total internal energy density $\tau_2 = \rho_2 \epsilon_2 + \rho_2 v_2^2/2$ and electron fraction Y_e :

$$\begin{aligned}\partial_t \tau_2 + \nabla \cdot [\alpha (\tau_2 + P_2) \vec{v}_2] &= -\alpha \rho_2 \vec{v}_2 \cdot \nabla \Phi, \\ \partial_t (\rho_2 Y_e) + \nabla \cdot (\alpha \rho_2 Y_e \vec{v}_2) &= 0.\end{aligned}\quad (8)$$

The gravitational potential Φ is solved by a multipole solver, for which we adopt the one by [Couch et al. \(2013\)](#) that can reduce error due to computing the potential at the cell center while using the mass density at that point. To mimic general relativistic strong-field effects, we use the modified case A potential ([Müller et al. 2008](#)) as an additional correction to the Newtonian potential. The correction reads:

$$\begin{aligned}\Phi &\rightarrow \Phi - \langle \Phi \rangle + \Phi_{\text{TOV},1} + \Phi_{\text{TOV},2}, \\ \langle \Phi \rangle &= -4\pi \int_0^\infty dr' r'^2 \frac{\langle \rho_1 + \rho_2 \rangle}{|r - r'|}.\end{aligned}\quad (9)$$

Here, r is the radial distance and $\langle \rho_1 + \rho_2 \rangle$ represent the angular average of the total density. $\Phi_{\text{TOV},i}$ for $i = 1, 2$ are the relativistic corrections:

$$\begin{aligned}\Phi_{\text{TOV},i} &= -4\pi \int_0^\infty \frac{dr'}{r'^2} \frac{1}{\Gamma_i^2} \left(\frac{m_{\text{TOV},i}}{4\pi} + r'^3 P_i \right) \\ &\quad \left(1 + \epsilon_i + \frac{P_i}{\rho_i} \right), \\ m_{\text{TOV},i} &= 4\pi \int_0^r dr' r'^2 \Gamma_i \rho_i (1 + \epsilon_i), \\ \Gamma_i &= \sqrt{1 + v_{r,i}^2 - \frac{2m_{\text{TOV},i}}{r}}.\end{aligned}\quad (10)$$

Where $v_{r,i}$ is the radial velocity. We adopt a finite-volume approach to solve the hydrodynamic equation in spherical coordinates ([Mignone 2014](#)). We use the piecewise parabolic method ([Colella & Woodward 1984](#)) to reconstruct primitive variables at the cell interface. We use the HLLC Riemann solver ([Toro 2009](#)) to compute fluxes across cell boundaries. The reconstruction and

fluxes evaluation is done on a dimension-by-dimension basis. We discretize the temporal evolution using the method of lines where the strong stability-preserving 5-step, 5th-order Runge-Kutta method is implemented (Gottlieb et al. 2011). In addition to the (modified) Euler equation, we also append the internal energy equation for the NM:

$$\partial_t(\rho_2 \epsilon_2) + \nabla \cdot \{\alpha[(\rho_2 \epsilon_2) + P_2] \vec{v}_2\} = \vec{v}_2 \cdot \nabla(\alpha P_2) - \alpha P_2(\vec{v}_2 \cdot \nabla \Phi). \quad (11)$$

And it not only allows one to interpolate internal energy density ϵ to the cell interface directly so that computational cost due to evaluating ϵ at the cell interface could be reduced, but it also reduces the error of ϵ due to advection (Zingale et al. 2020). We adopt a computational grid similar to Skinner et al. (2016), in which the analytic function describes the position of the radial cell interface as:

$$r = A_t \sinh(x_t i / A_t). \quad (12)$$

Here, i is the cell index. We set $x_t = 0.5$ and $A_t = 150$ so that a central resolution of around 0.34 km is provided, while a total of 500 computational grid is used to contain the progenitor. We set the angular resolution to be 20, where we find this value is sufficient to ensure convergence in GW signals for both the NM and DM.

2.4. Micro-physics

After mapping the density profiles of the NM and DM component computed from Section 2.1, we assign a temperature profile to the NM (Dessart et al. 2006):

$$T(\rho) = T_c(\rho/\rho_c)^{0.35}. \quad (13)$$

Here, T_c is the central temperature and ρ_c is the central density. We implement the parameterized electron capture scheme described in Liebendorfer (2005). Y_e depends on ρ_2 as:

$$x(\rho_2) = \max \left[-1, \min \left(1, \frac{2 - \log \rho_2 - \log \rho_\alpha - \log \rho_\beta}{\log \rho_\alpha - \log \rho_\beta} \right) \right],$$

$$Y_e(x) = \frac{1}{2}(Y_b + Y_a) + \frac{x}{2}(Y_b - Y_a) + Y_c[1 - |x| + 4|x|(|x| - 1/2)(|x| - 1)]. \quad (14)$$

Here, $\log \rho_\alpha$, $\log \rho_\beta$, Y_a , Y_b , and Y_c are fitting parameters and are obtained by Leung et al. (2019) and Zha et al. (2019a). We assign an equilibrium Y_e profile to the NM using Equation 14. We then start the electron capture process by updating Y_e at each time step using the same equation. We force Y_e to be strictly decreasing with time. We terminate the electron capture process

once the core bounce condition is achieved. We follow Liebendorfer (2005) to define the core bounce condition to be the core NM entropy larger than $3k_B$, where k_B is the Boltzman constant.

2.5. Gravitational-wave Signals

We use the quadruple formula in the weak-field approximations to compute the GW strain (Finn & Evans 1990; Moenchmeyer et al. 1991):

$$h_+ = \frac{3}{2} \frac{G}{Dc^4} \sin^2 \theta \frac{d^2}{dt^2} I_{zz}. \quad (15)$$

Here, $D = 10$ kpc is the distance, and θ is the orientation to the collapsing DMRWD. I_{zz} is the moment of inertia tensor:

$$I_{zz} = \frac{1}{3} \int_{\text{All Space}} (\rho_1 + \rho_2) r^2 P_2(\cos \theta) d\tau. \quad (16)$$

2.6. Equations of State

To simulate AICs, we would first use the ideal degenerate Fermi gas EOS for equilibrium structure constructions. Following the subsequent collapse dynamics, we use the nuclear matter EOS given by Shen et al. (1998), widely used in simulating core-collapse supernovae and neutron star dynamics. We adopt the ideal degenerate Fermi gas EOS for the DM component (Narain et al. 2006).

3. RESULTS AND DISCUSSION

We define \bar{t} as the time after the NM core bounce to facilitate discussions. We terminate all our simulations at $\bar{t} = 0.1$ s.

3.1. The Diffusive Dark Matter Limit

We have computed a series of DMRWD models as DMAIC progenitors. The stellar parameters of these progenitors have been listed in Table 1 for reference. The progenitors have increasing DM mass fractions ϵ from 0.01 to 0.2. The progenitors include rigidly-rotating and differentially-rotating DMRWD with different d as described in Equation 4. In particular, d is chosen so that $\rho_2(r = d, \theta = \frac{\pi}{2}) = \alpha_d \rho_{2c}$. We choose $\alpha_d = 0.1$ and 0.01. Another free parameter to be specified for these progenitors is the central angular velocity Ω_c . We adjust this value for rigidly-rotating DMRWDs so that the corresponding pure NM progenitor almost rotates at the Keplerian limit and that a total mass of $\approx 1.8 M_\odot$ is achieved for a pure NM, differentially rotating WD. We fix the DM particle mass to be 0.1 GeV for all of these progenitors. As shown in Chan et al. (2021), the fluid component formed by DM particle with such mass will be more diffusive and comparable to that of the NM.

3.1.1. The Collapse Dynamics

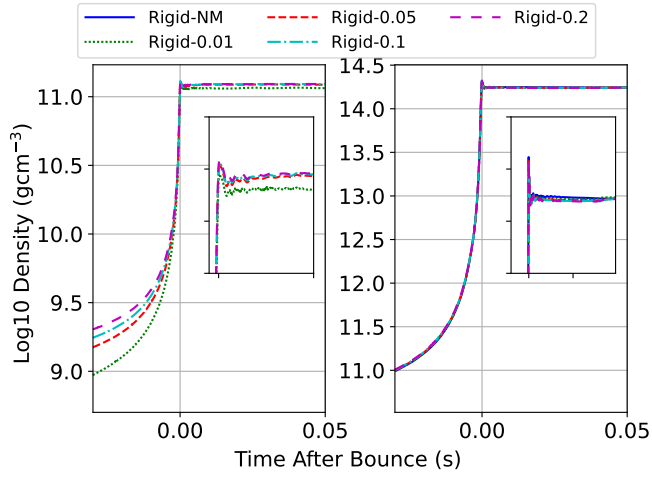


Figure 1. The maximum densities evolution for the rigidly-rotating DMAIC models. The left- (right-) hand panel is for DM (NM). Since there are only minimal deviations with respect to different DM-admixed models, we tabulated magnified density evolution plots in each panel for better illustrations.

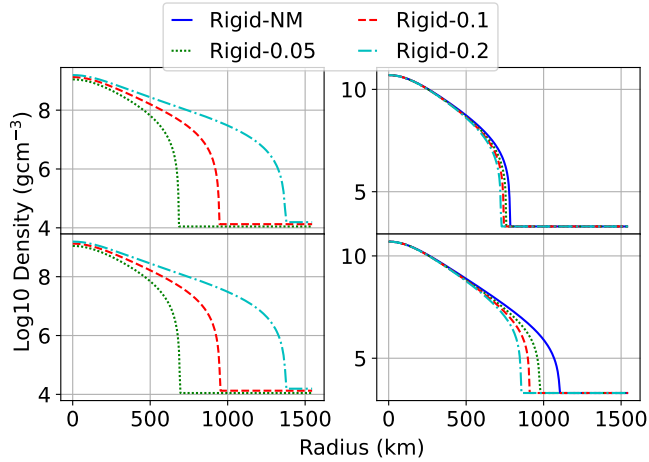


Figure 2. The initial density profiles for the rigidly-rotating DMAIC progenitors. The left- (right-) hand panel is for DM (NM). The upper (lower) sub-panel in each panel is for the polar (equatorial) density profiles.

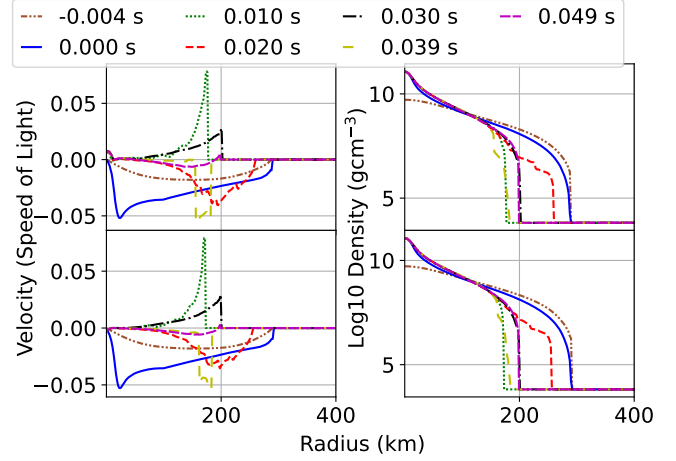


Figure 3. The DM radial density and velocity profile evolution for different \bar{t} of the Rigid-0.01 DMAIC model. The left- (right-) hand panel is for the velocity (density). The upper (lower) sub-panel in each panel is for the polar (equatorial) profiles.

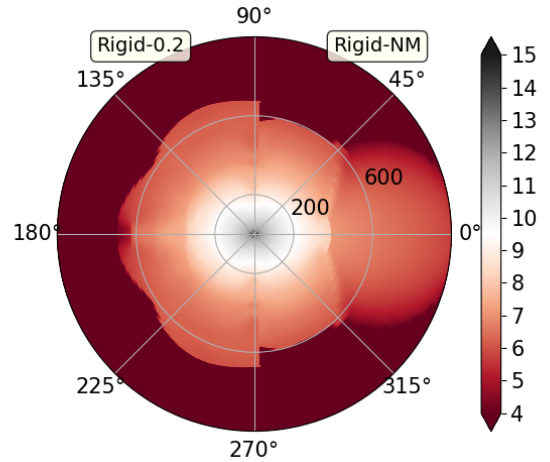


Figure 4. The NM density contour plot for two different rigidly-rotating DMAIC models at the end of the simulations. The right- (left-) hand plot is for the Rigid-NM (Rigid-0.2) model. Densities are in the \log_{10} scale of gcm^{-3} . The radial distance is in km.

We first focus on the collapse dynamics of DMAIC. From Table 1, we observe that the admixture of DM delays the time of bounce. And this is because the admixture of DM reduces the NM mass, so the NM component experiences less gravitational pull. We show the maximum NM density evolution for the rigidly-rotating DMAIC models in the right-hand panel of Figure 1. Despite having different initial and proto-neutron star

masses (c.f. Table 1), the maximum NM density evolution is almost identical for all DMAIC models. The final maximum NM densities are also insensitive to the DM mass fractions ϵ . Furthermore, we find that AIC is successful for all DMAIC progenitors. And this is in contrast to the results presented by Leung et al. (2019) and Zha et al. (2019a). The disagreement between our results and theirs is because we are assuming different DM particle masses. Their work assumed a heavy (1 GeV) DM particle mass, where the DM component is more compact and has a large central density. Thus,

Table 1. The stellar parameters for different DMAIC progenitors. They include rigid (models with Rigid) and differentially (models with Kepler) rotating DMRWDs. All progenitors have NM central density of $5 \times 10^9 \text{ gcm}^{-3}$. The DM particle mass is 0.1 GeV.

Model	M_{NM}	M_{DM}	α_d	$\log_{10}\rho_{1c}$	Ω_c	R_{eNM}	R_{eDM}	ϵ_{DM}	t_b	$\log_{10}\rho_{1b}$	$\log_{10}\rho_{2b}$	M_{PNS}
-	(M_{\odot})	(M_{\odot})	-	(gcm^{-3})	(s^{-1})	(km)	(km)	-	(ms)	(gcm^{-3})	(gcm^{-3})	(M_{\odot})
Rigid-NM	1.477	0.000	-	-	10.8	1105	-	0	53.151	-	14.318	1.217
Rigid-0.01	1.447	0.015	-	8.816	10.8	1098	400	0.01	53.424	11.078	14.317	1.194
Rigid-0.03	1.416	0.044	-	8.980	10.8	1027	568	0.03	53.717	11.093	14.315	1.170
Rigid-0.05	1.397	0.074	-	9.046	10.8	980	695	0.05	53.902	11.097	14.316	1.157
Rigid-0.07	1.384	0.104	-	9.086	10.8	948	807	0.07	54.035	11.100	14.315	1.146
Rigid-0.09	1.374	0.136	-	9.114	10.8	923	904	0.09	54.139	11.102	14.315	1.139
Rigid-0.1	1.307	0.152	-	9.125	10.8	910	954	0.1	54.183	11.103	14.315	1.136
Rigid-0.2	1.343	0.336	-	9.193	10.8	857	1379	0.2	54.496	11.107	14.313	1.119
Kepler-NM-d001	1.770	0.000	0.01	-	32.5	1826	-	0	35.124	-	14.355	1.597
Kepler-0.01-d001	1.725	0.017	0.01	8.853	32.5	1766	420	0.01	35.352	11.073	14.352	1.553
Kepler-0.03-d001	1.662	0.051	0.01	9.016	32.5	1494	587	0.03	35.647	11.086	14.351	1.498
Kepler-0.05-d001	1.623	0.085	0.01	9.082	32.5	1343	710	0.05	35.835	11.091	14.352	1.463
Kepler-0.07-d001	1.596	0.120	0.01	9.122	32.5	1256	812	0.07	35.969	11.094	14.350	1.439
Kepler-0.09-d001	1.577	0.156	0.01	9.150	32.5	1190	904	0.09	36.072	11.096	14.350	1.419
Kepler-0.1-d001	1.569	0.174	0.01	9.162	32.5	1159	948	0.1	36.116	11.097	14.350	1.411
Kepler-0.2-d001	1.518	0.379	0.01	9.232	32.5	1020	1352	0.2	36.424	11.101	14.349	1.362
Kepler-NM-d001	1.771	0.000	0.1	-	45.2	1106	-	0	32.311	-	14.354	1.598
Kepler-0.01-d01	1.727	0.017	0.1	8.860	45.2	1098	417	0.01	32.555	11.070	14.353	1.555
Kepler-0.03-d01	1.677	0.052	0.1	9.026	45.2	1062	579	0.03	32.788	11.084	14.354	1.511
Kepler-0.05-d01	1.647	0.087	0.1	9.094	45.2	1034	700	0.05	32.924	11.088	14.351	1.483
Kepler-0.07-d01	1.625	0.122	0.1	9.135	45.2	1007	801	0.07	32.024	11.092	14.351	1.460
Kepler-0.09-d01	1.609	0.159	0.1	9.164	45.2	987	892	0.09	33.101	11.095	14.352	1.446
Kepler-0.1-d01	1.602	0.178	0.1	9.176	45.2	980	941	0.1	33.133	11.096	14.352	1.439
Kepler-0.2-d01	1.556	0.389	0.1	9.247	45.2	916	1343	0.2	33.364	11.101	14.355	1.396

NOTE—In this table, R_{eNM} (R_{eDM}) is the equatorial radius of the progenitors for the NM (DM) component. ρ_{1c} is the DM central density, ϵ_{DM} is the DM fraction, and t_b is the bounce time. ρ_{2b} (ρ_{1b}) is the maximum NM (DM) density at core bounce. M_{PNS} is the proto-neutron star mass, defined as summing all the NM mass with $\rho_2 > 10^{11} \text{ gcm}^{-3}$ at the end of the simulations.

it significantly impacts the NM density profile near its centre. The NM density decreases sharply due to the strong gravitational force provided by the compact DM core. Electron capture is less efficient, so the NM component's effective adiabatic index remains near $\frac{4}{3}$. We assumed a light (0.1 GeV) DM particle mass in our study. The DM component is more diffusive and extended. Hence it brings a less significant impact to the NM density profile near its core. We demonstrate the NM density profile changes with increasing DM mass fractions ϵ in the right-hand panel of Figure 2. We observe that when more DM is admixed, the changes in NM density profiles are primarily at the outer envelope. The core of the NM component remains almost unchanged. The collapse dynamics of a WD are gov-

erned by the densest core, where ρ_2 is large enough to initiate electron capture. Since the core NM density profile changes are insensitive to the DM mass fractions ϵ in our study, it is natural to expect generic collapse dynamics for all rigidly-rotating DMRWDs.

We discovered that the DM component collapses with the NM component to form a bound DM core. We show the DM density profile evolution in the left-hand panel of Figure 3. We found that the DM densities evolve similarly to the NM densities. The DM densities also remain stable after the NM core bounce. We show the density profile evolution for a particular model Rigid-0.01 in the right-hand panel of Figure 3 as an example. The DM radius contract from $\sim 350 \text{ km}$ at $\bar{t} = 0.014 \text{ s}$, to ~ 180

km at $\bar{t} = 0.01$ s. Although the DM radius increases at $\bar{t} = 0.02$ s, the DM component gradually contracts to ~ 200 km at $\bar{t} = 0.03$ s and pulsate around $\sim 180 - 200$ km. And this suggests that a bound DM component has formed with negligible mass loss. Since the DM collapse dynamics are similar to those of the NM, it is natural to expect a post-bounce shock wave for the DM component. We show the DM velocity profile evolution of the same DMRWD model in the left-hand panel of Figure 3. The post-bounce velocity shock breakthrough the DM surface around $\bar{t} = 0.01$ s. However, the velocity shock is too weak to unbind the DM component. The strength of the velocity shock gradually reduces and becomes a sound wave that propagates inside the DM component. This also explains the pulsation of the DM component between $\bar{t} = 0.03$ and 0.049 s.

3.1.2. The Formation of Dark Matter-admixed Neutron Stars

What are the astrophysical implications of our findings? DM-admixed neutron stars have been extensively studied in the past decade. For instance, Bhat & Paul (2020) showed that the admixture of DM can explain the cooling rate of some pulsars/neutron stars, e.g., PSR B0656+14, PSR B1706-44 and PSR B2334+61, which could not be explained if the popular APR equation of state (EOS) is assumed. Das et al. (2021) and Lee et al. (2021) explain the anomalous $2.6 M_\odot$ object from the gravitational-wave event GW190814 (Abbott et al. 2020) by the DM-admixed neutron star model. However, the formation channel of DM-admixed neutron stars has never been addressed in depth. Although Zha et al. (2019b) performed DMAIC simulations, their work relies on the assumption that the DM is compact and non-movable. This assumption, however, does not always hold. Our self-consistent, two-fluid simulations show that the AIC of a DMRWD would produce a DM-admixed (rotating) neutron star, such that the DM component is gravitationally bound with negligible mass loss. The collapse of DM also happens with a time scale similar to that of NM. Therefore, we have shown numerically that it is possible to form a DM-admixed neutron star through DMAIC.

3.1.3. Gravitational-wave Signatures

The non-luminous nature of the DM makes it difficult to be detected through conventional telescopes. The weak electromagnetic signatures from a typical AIC also hinder indirect DM detection by comparing AIC luminosities. Therefore, we rely on predicting the GW signatures generated by both the NM and DM components.

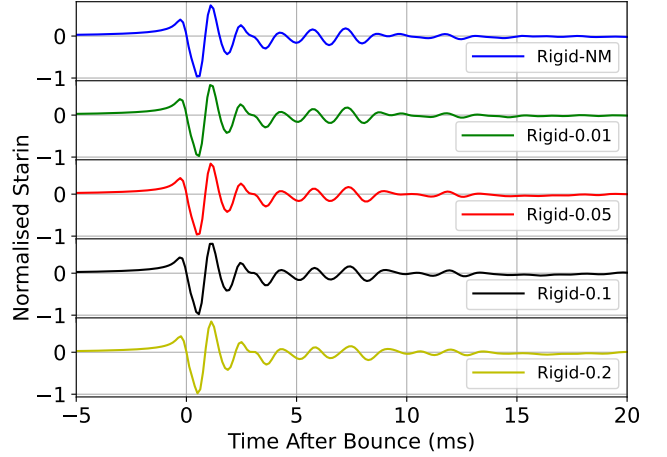


Figure 5. The total GW strains for the rigidly-rotating DMAIC models. We normalised all the GW strains to the corresponding maximum amplitude of the Rigid-NM model. The normalisation constant is 7.53×10^{-21} .

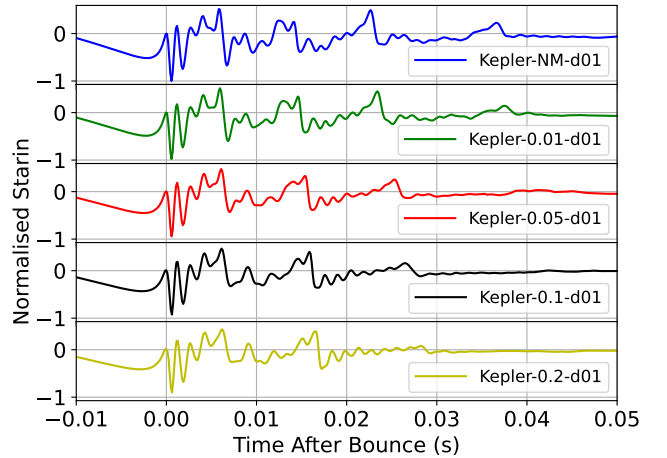


Figure 6. Same as Figure 5, but for the Kepler-rotating and $\alpha_d = 0.1$ models with a normalisation constant of 5.05×10^{-21} .

Equation 14 suggests the moment of inertia tensor I_{zz} is separable into individual DM and NM components:

$$I_{zz} = I_{zz,1} + I_{zz,2},$$

$$I_{zz,i} = \frac{1}{3} \int_{\text{All Space}} \rho_i r^2 P_2(\cos\theta) d\tau. \quad (17)$$

Since DM only interacts with NM through gravity, the Euler equations for the DM component do not contain any non-trivial NM-related terms except the gravitational potential Φ . Hence, the GW signature from the AIC of a DMRWD can be separated into the DM and

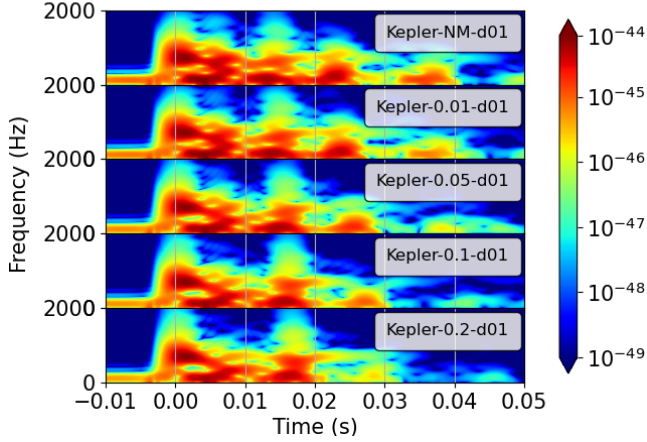


Figure 7. Power spectral density of DMAIC GWs for DM-RWD rotating in the Kepler rule with $\alpha_d = 0.1$.

Table 2. GW mismatch with respect to the pure NM model for DMAIC with different initial rotation profiles. See Table 1 for the simulation parameters of these models.

-	Rigid	Kepler-d001	Kepler-d01
DM-0.01	0.306	13.570	19.217
DM-0.03	0.870	26.151	42.386
DM-0.05	1.263	29.103	41.173
DM-0.07	1.596	36.149	41.169
DM-0.09	1.844	38.256	44.517
DM-0.1	1.992	40.916	43.785
DM-0.2	2.784	41.845	52.794

NOTE—The mismatch here is given as in units of percentage.

NM contributions:

$$h_+ = h_{+,1} + h_{+,2}, \quad (18)$$

$$h_{+,i} = \frac{3}{2} \frac{G}{Dc^4} \sin^2 \theta \frac{d^2}{dt^2} I_{zz,i}.$$

To compute $h_{+,i}$, we can make use of Equation (16) in Ott et al. (2004), and substitute all the components of \vec{v} and ρ by the corresponding DM/NM value.

It is also a common practice to study GW strains by time-frequency analysis. To obtain the GW spectrograms, we perform a windowed Fourier transform:

$$\tilde{h}^*(f, t) = \int_{-\infty}^{\infty} h_+(\tau) w(t, \tau) \exp(-2\pi i f \tau) d\tau \quad (19)$$

Here, $w(t, \tau)$ is the window function, and we choose it as the Hann window.

We first show the AIC GWs generated by the rigidly-rotating DMRWD models in Figure 5. The GWs are all generic Type I waveforms (Fryer & New 2011). There are no considerable differences in the GW signature with respect to all DM-admixed models. This is in contrast to the results presented by Zha et al. (2019b), where they show enhanced amplitudes during $\bar{t} = 0$. And this is because the contributions to the GW strains are mainly from the innermost core (~ 10 km). We have shown in the previous section that the effects of admixing 0.1 GeV DM on the NM density profile are mainly at the NM outer envelope. The NM collapse dynamics are also generic for all DM-admixed models. We append the NM density contour plots of model NM-Rigid and DM-Rigid-0.2 in Figure 4 as references. We observe that the densest core, which corresponds to the major part of the proto-neutron star, of the DM-admixed model is almost identical to that of the pure NM counterpart. And this explains why the GW signatures from rigidly-rotating DMRWDs are all generic.

However, the situation is different for differentially rotating progenitors. We show the GW strains of the Kepler-rotating and $\alpha_d = 0.1$ model in Figure 6. We find that the admixture of DM indirectly suppresses the post-bounce 3rd and 4th peaks of the GW strains. And this could also be observed as the gradual disappearance of the 3rd and 4th spectral peaks in Figure 7. Therefore, the GW strains of DMAIC are qualitatively different from that of the pure NM model. We find that the spectral peak exists for the pure NM model because the reflected shock waves pass through the NM core and makes it pulsate non-radially. The corresponding pulsation for the DM-admixed models is smaller, resulting in a weaker GW signature. We find similar results for the Kepler-rotating and $\alpha_d = 0.01$ model, except that the 4th spectral peak never exists for the pure NM and hence, the DM-admixed models.

The DM component is more diffusive for fermionic DM with a particle mass of 0.1 GeV. As such, the collapse dynamics of the DM component could not produce GW signatures comparable to that of the NM component. The effects of DM admixture on the total signatures are, therefore, indirect. To quantitatively determine whether such effects could be observable, we compute the mismatch \mathfrak{M} , which quantifies how similar/dissimilar two waveforms are (Reisswig & Pollney 2011; Richers et al.

2017):

$$\mathfrak{M} = 1 - \max \left(\frac{\langle h_a, h_b \rangle}{\sqrt{\langle h_a, h_a \rangle \langle h_b, h_b \rangle}} \right) \quad (20)$$

The second term here is the match between two waveforms h_a and h_b :

$$\langle h_a, h_b \rangle = \int_0^\infty \frac{4\tilde{h}_a^* \tilde{h}_b}{s} df \quad (21)$$

Here, s is the estimated noise amplitude spectral density of the Advanced LIGO, for which we take that given by Barsotti et al. (2018). \tilde{h}^* is the Fourier transform of the GW strain, which is just Equation 19 but with $w(t, \tau) = 1$. The mismatch is maximized over the relative phase, amplitudes, and arrival times. We follow Zha et al. (2019b) to set the integration limit of Equation 21 to be from 100 Hz to 2000 Hz. The computations are facilitated through the open-source package PyCBC (Nitz et al. 2022). We extract GW waveforms for all the models listed in Table 1 with a time window of $-0.01 < \bar{t} < 0.05$ s, and compute the mismatches with respect to the pure NM model. We list the results in Table 2. We notice that the mismatch for the rigidly-rotating DMAIC models is small, which is no surprise because the GW waveforms of the DM-admixed model in such a scenario are very similar to that of the pure NM counterpart. The mismatch for the Kepler-rotating DMAIC models, however, is large. And this might be because the DM admixture significantly affects the GW frequency spectrum. We claim that the presence of a 1 % of DM can be inferred from future GW detection produced by DMAIC, given that Advanced LIGO can distinguish two waveforms with an accuracy better than 14 %.

3.2. The Compact Dark Matter Limit

The properties of a compact star with a fermionic DM had shown to be sharply changing around DM particle mass of 0.1 GeV (Leung et al. 2022). To better capture the transitional effects from a sub-GeV to GeV mass, we include progenitor models admixed with fermionic DM of particle mass 0.3 GeV. Furthermore, the progenitor are all differentially-rotating DMRWD with $\alpha_d = 0.5$. For reference, we include the parameters of our appended models in Table 3. We generally find similar collapse dynamics for the DM and NM components as those of the diffusive DM limit. For instance, we find a delay in the NM bounce time and the successful formation of a DM-admixed neutron star. The in-depth discussion of the collapse dynamics of DMAIC under the compact DM limit would therefore be omitted.

3.2.1. Gravitational Waves from the Dark Matter Component

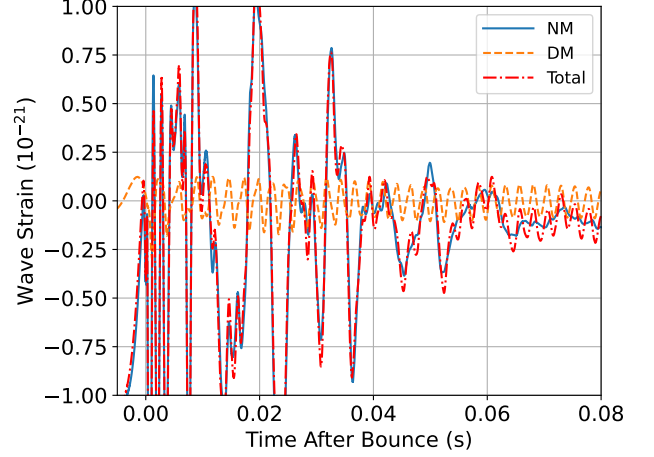


Figure 8. The magnified plot of the NM, DM and total GW strains for the Kepler-0.05-d05 model.

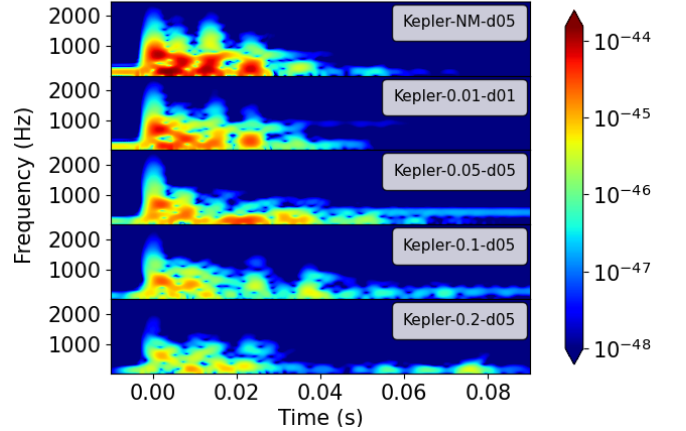


Figure 9. Same as Figure 7, but for DMRWD rotating in the Kepler rule with $\alpha_d = 0.5$.

In this section, we focus on the GW signature produced by the DMAIC event. As an example, we show the GW strains of a particular model Kepler-0.05-d05 in Figure 8. We discover that the DM GW strain has amplitudes comparable to that of the NM. The DM GW signature directly adds to the total GW strain, producing secondary oscillation on top of the NM GW strain. And this is in contrast to the diffusive DM limit. With increasing DM particle mass, the DM becomes more compact. Furthermore, the NM component has a $\alpha_d = 0.5$, which represent highly differentially-rotating configurations. The DM component reacts to the highly

Table 3. Same as Table 1, but for differentially rotating DMAIC progenitors that have $\alpha_d = 0.5$ and the DM particle mass to be 0.3 GeV.

Model	M_{NM}	M_{DM}	α_d	$\log_{10}\rho_{1c}$	Ω_c	R_{eNM}	R_{eDM}	ϵ_{DM}	t_b	$\log_{10}\rho_{1b}$	$\log_{10}\rho_{2b}$	M_{PNS}
-	(M_\odot)	(M_\odot)	-	(gcm^{-3})	(s^{-1})	(km)	(km)	-	(ms)	(gcm^{-3})	(gcm^{-3})	(M_\odot)
Kepler-NM-d05	1.771	-	0.5	-	45.2	916	-	0.00	29.087	-	14.351	1.604
Kepler-0.01-d05	1.672	0.017	0.5	9.968	45.2	929	157	0.01	30.595	12.720	14.345	1.516
Kepler-0.03-d05	1.525	0.047	0.5	10.206	45.2	948	187	0.03	32.426	12.826	14.339	1.379
Kepler-0.05-d05	1.410	0.074	0.5	10.313	45.2	961	202	0.05	33.778	12.856	14.336	1.267
Kepler-0.07-d05	1.313	0.099	0.5	10.383	45.2	967	212	0.07	34.899	12.866	14.332	1.170
Kepler-0.09-d05	1.229	0.122	0.5	10.434	45.2	967	220	0.09	35.888	12.871	14.332	1.090
Kepler-0.1-d05	1.191	0.132	0.5	10.454	45.2	967	223	0.1	36.348	12.873	14.333	1.052
Kepler-0.2-d05	0.896	0.224	0.5	10.588	45.2	935	246	0.2	40.396	12.872	14.331	0.767

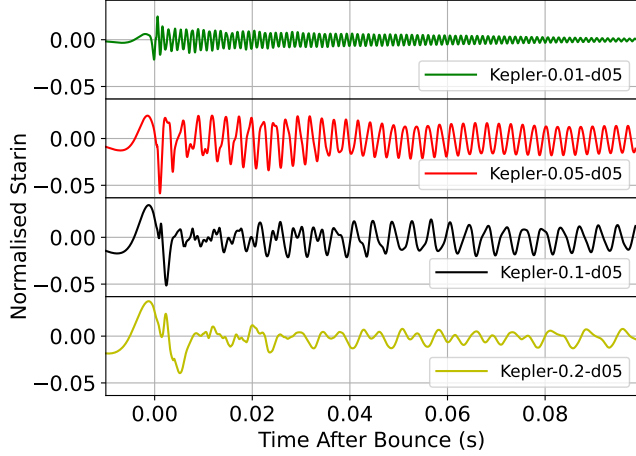


Figure 10. Same as Figure 5, but for the DM GWs of the Kepler-rotating DMAIC models with $\alpha_d = 0.5$ only. The normalisation constant is 6.07×10^{-21} .

deformed NM component to become a spheroid. The vigorous non-spherical collapse dynamics thus generate a considerable magnitude of GWs. We analyze the GW strains by plotting their spectrograms in Figure 9. We find that the admixture of DM greatly suppresses the NM GW strains around the NM core bounce, which is of no surprise because the NM content is reduced substantially when DM is admixed (c.f. Table 3). We also find that the DM GW strains could be captured as continuous low-frequency (< 1000 Hz) signature in the spectrogram before $\bar{t} = 0.1$. And this is an important finding because prompt convection can also generate low-frequency signals after the NM bounce, but it was found that such convection-related GW signals happen after $\bar{t} = 0.1 - 0.2$ (Zha 2019). Therefore, any low-frequency signals observed before $\bar{t} = 0.1$ could be a direct evidence of compact DM admixture. We close

this discussion by showing the DM GW waveforms in Figure 10. We observe that the DM GWs are consistent with the Type III collapsing polytrope waveforms presented in Fryer & New (2011).

3.2.2. Detection Prospect

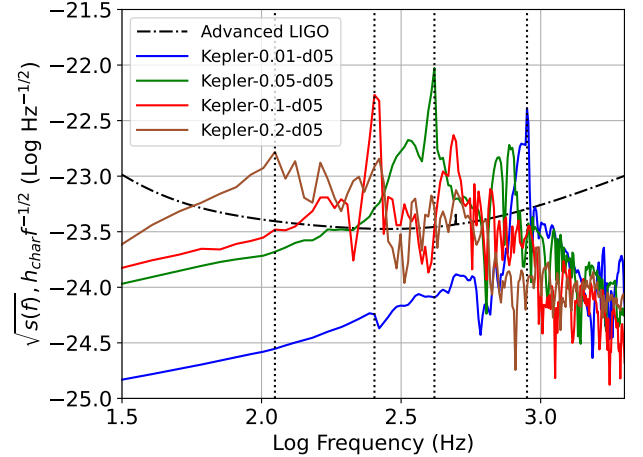


Figure 11. The scaled characteristic DM GW strains for the differentially-rotating DMAIC models with $\alpha_d = 0.5$. In the same figure, we mark the peak frequency from the Fourier transform amplitude as vertical black dotted lines.

In the last section, we show that the DM GW signatures are strong enough to influence the total GW strains directly. What would be their detectability? We compute the dimensionless characteristic GW strain (Flanagan & Hughes 1998):

$$h_{\text{char}} = \sqrt{\frac{2}{\pi^2} \frac{G}{c^3} \frac{1}{D^2} \frac{dE_{\text{GW}}}{df}} \quad (22)$$

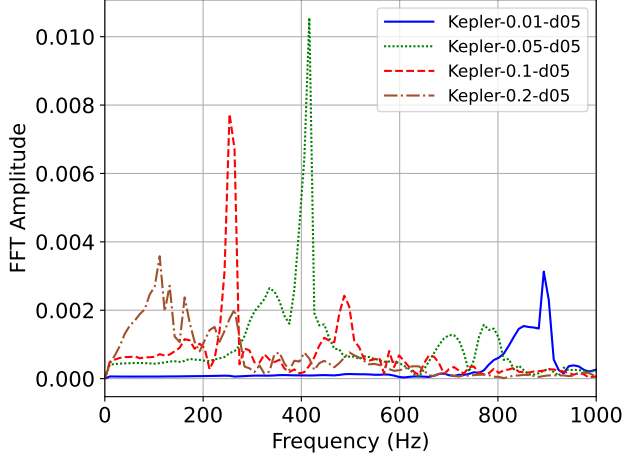


Figure 12. The fast Fourier transform amplitude of the DM GWs against frequency for 4 different DMAIC models with $\alpha_d = 0.5$.

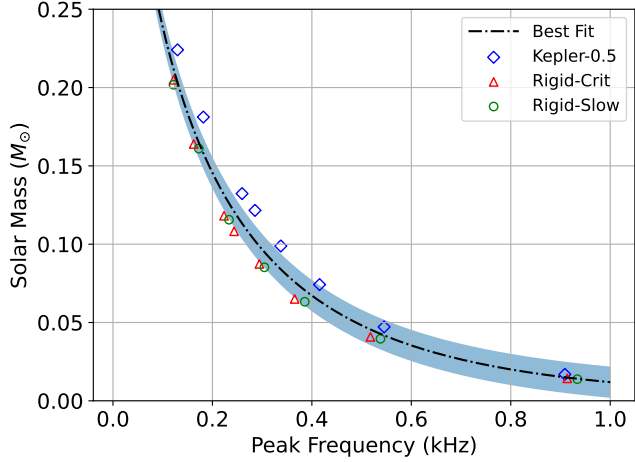


Figure 13. The DM mass against GW peak frequency for DMAIC with a DM particle mass of 0.3 GeV. Note that we include differentially (Kepler-0.5), rapidly rigid (Rigid-Crit), and slowly rigid (Rigid-Slow) rotating progenitors. The black dash-dotted line represents the best fit curve as stated in Equation 24, and the blue strip is the mean-absolute error of our fitting.

Here, $\frac{dE_{\text{GW}}}{df}$ is the GW spectral energy (Murphy et al. 2009):

$$\frac{dE_{\text{GW}}}{df} = \frac{3}{5} \frac{G}{c^5} (2\pi f)^2 |\tilde{h}_+|^2 \quad (23)$$

We compare $h_{\text{char}} f^{-1/2}$ with the Advanced LIGO noise spectral density $\sqrt{s(f)}$ and show them in Figure 11. In the same figure, we mark vertical lines corresponding to the peak frequency obtained by performing a fast Fourier transform on the DM GW waveforms. We choose the sampling window to be $\tilde{t} > 0$. For reference, we also present the Fourier transform results in Figure

12. We find that the DM characteristic GW strain corresponds to the frequency peak lying above the Advanced LIGO sensitivity curve, which is true for all of our considered models. Note that we have set $D = 10$ kpc, roughly the Milky-way's radius. Hence, the GW signature of a collapsing, compact DM in a DMAIC event should be detectable by Advanced LIGO, provided that it happens within the Milky-way. Our results would also be the first-ever numerical calculation of the GW waveforms of a collapsing DM.

We discovered that the DM GW peak frequency is reduced when the DM fraction is increased. We show this trend in Figure 13. Note that in the figure, we include data points extracted from simulations with Kepler-rotating (Kepler-0.5), rapidly rigid (Rigid-Crit), and slowly rigid (Rigid-Slow) rotating progenitors. In particular, rapidly rigid rotating models have an angular velocity of 0.97 that of the critical velocity, and slowly rigid rotating models have $\Omega_c = 1$ rad s⁻¹. The figure shows a relationship between the DM mass and its peak frequency. We fit the relation by:

$$M_1 = 0.572 \exp(-3.873 f_1^{0.646}) \quad (24)$$

Here, M_1 is the DM mass in solar mass, and f_1 is the DM GW peak frequency in kHz. The relation is valid for $\sim 100 - 1000$ Hz. Note that we include differentially rotating, as well as rapid and slowly but rigidly rotating models in fitting this relation. Therefore, this relation should be model-independent, provided that the DM particle mass is 0.3 GeV. From the application aspect, one can (as we proved that it is possible to) directly detect DM GWs from AIC events. Then, one can infer the DM GW peak frequency from the raw signals. Equation 24 can then be applied to directly measure the amount of DM admixture, assuming the DM particle mass to be 0.3 GeV. The exploration of such relations for higher DM particle mass would be an interesting future study. Finally, we will show the detectability of DM GWs from rigidly rotating progenitors in Appendix B.

4. CONCLUSION

We presented two-dimensional simulations of DMAIC with self-consistent modeling of the DM dynamics. Regardless of the DM particle mass and compactness, the DM component will follow the collapse of the NM component to become a bound DM core with a time scale comparable to that of the NM. Such a result demonstrated numerically, for the first time, how a DM-admixed neutron star could form through DMAIC. Despite such novel findings, we find similar results to those by Leung et al. (2019) and Zha et al. (2019a), such

as the delay of the NM bounce time and the reduction of the proto-neutron star mass.

Due to the weak electromagnetic signatures produced by the gravitational collapse of WDs, GW becomes an important and reliable channel to detect and study AIC. We computed the GW signature for both the NM and DM component using the quadruple formula. For DM with a particle mass of 0.1 GeV, the DM component is more diffusive and extended. Hence, the collapse of the DM component does not produce a significant GW signature. However, the admixture of such DM indirectly influences the NM signature by suppressing the NM GW spectral peaks after the NM core bounce. The significant alteration of the NM GW frequency spectrum also makes the DMAIC waveforms easily to be detectable by GW detectors, which shows a 14 % mismatch when compared to the pure NM counterpart by admixing only 1 % of DM. For DM with a particle mass of 0.3 GeV, the DM component is more compact. The admixture of DM greatly reduces the NM mass and hence its compactness. The NM GW signature at bounce is therefore decreased substantially. However, we find that the DM component is massive and compact enough to produce a GW signature comparable to the NM counterpart during its dynamical collapse. The DM GW adds up to the NM GW to produce secondary oscillations. These oscillations could be seen as continuous low-frequency (< 1000 Hz) signals in the GW spectrograms. The oscillations happen at $\bar{t} < 0.1$ s, which is before the time of low-frequency GW induced by prompt convection. Hence, any low-frequency signals detected from an AIC event at $\bar{t} < 0.1$ s could be direct evidence of the existence of DM. We compare the characteristic GW strains of the DM component with the Advanced LIGO sensitivity curve, and we find that all the peak-frequency signals of the DM component are detectable by the Advanced LIGO, provided that the DMAIC event happens within the Milky-way. We also discover a model-independent relationship between the DM mass and GW peak frequency. We provide a fitting

function for such a relation, and the function could be used to directly measure the amount of DM admixture from the DM GW peak frequency. The function assumed the DM particle mass is 0.3 GeV and is valid for $f_1 \sim 100 - 1000$ Hz. Not only are our results the first-ever computations of GW from a collapsing DM, but these findings also provide the key features to identify DM in AIC events through future GW detections.

Despite having novel simulation results, our framework still has some flaws. First, we assumed the DM component to be non-rotating. In particular, we considered the DM to be the ideal degenerate Fermi gas. The effective quantum self-interaction allows DM to have collective motion, such as rotation. Although the low DM accretion rate suggests that no significant amount of angular momentum could be built up (Iorio 2010), we expect DM should carry some initial angular momentum during the molecular cloud collapse phase. Nonetheless, we assume the DM to be non-rotating for this exploratory study. Second, we omitted detailed neutrino-transport physics in the simulations. Whether the presence of DM would greatly influence neutrino-flavor production would be interesting to investigate, and if it does, it would also be another important DM-detecting channel. Lastly, we only include ad-hoc relativistic corrections to the gravity and dynamical equations. A more realistic picture of the collapse dynamics and the GW signature would rely on better treatment of the relativistic treatment, which would possibly include solving the dynamical equations in the full general-relativity framework.

ACKNOWLEDGMENTS

We thank Otto Akseli Hannuksela for his helpful discussion regarding gravitational-wave mismatch calculations. This work is partially supported by a grant from the Research Grant Council of the Hong Kong Special Administrative Region, China (Project No. 14300320). Shing-Chi Leung acknowledges support from NASA grants HST-AR-15021.001-A and 80NSSC18K1017.

APPENDIX

A. THE FORMATION OF DARK MATTER-ADMIXED WHITE DWARF

We follow Chan et al. 2022 (submitted) to consider the progenitor of DMRWD to be a star born with an inherent admixture of DM. We assume the DM and NM to be spherically symmetric clouds having constant densities ρ_1 and ρ_2 , respectively. We consider the situation with the DM radius R_1 being larger than that of the NM, R_2 . The total

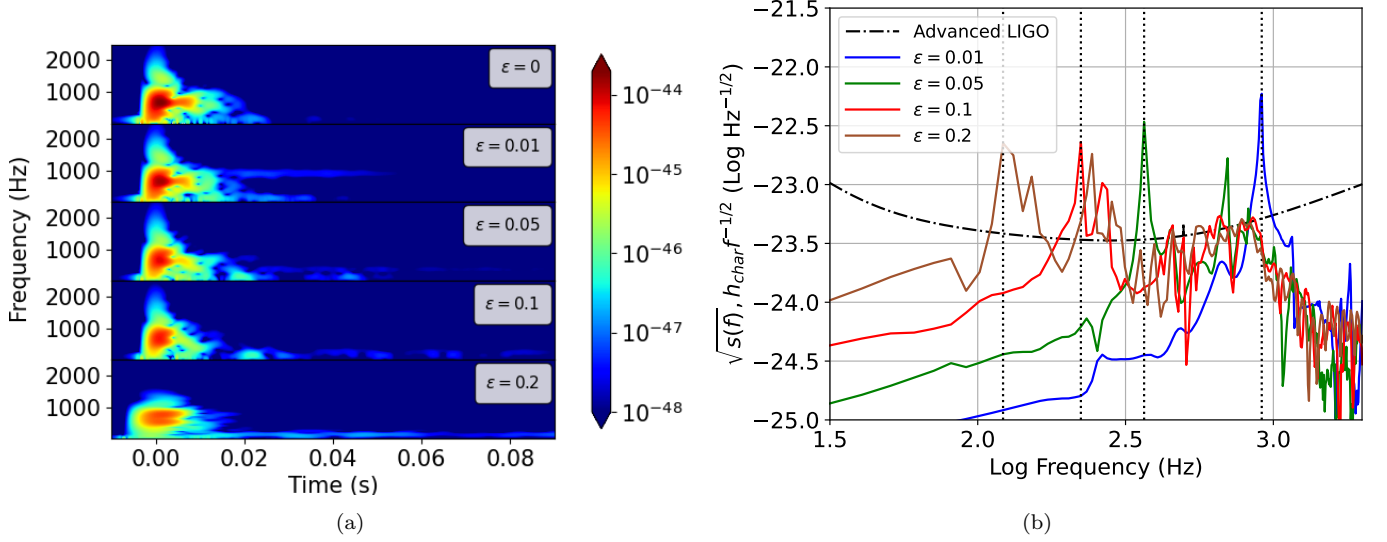


Figure 14. (a) Power spectral density of DMAIC GWs for rigidly-rotating progenitors with increasing DM mass fraction ϵ . (b) Same as Figure 11, but for characteristic wave strains of models presented in (a) and their comparison with the Advanced LIGO sensitivity curve.

energy E is:

$$E = -\left(\frac{3}{5} \frac{GM_1^2}{R_1} + \frac{3}{5} \frac{GM_2^2}{R_2} + \frac{3}{2} \frac{GM_1 M_2}{R_1} - \frac{3}{10} \frac{GM_1^2 R_1^2}{R_1^3}\right) + \frac{3}{2} NkT + \frac{1}{2} M_1 v_1^2. \quad (\text{A1})$$

Here, v_1 is the DM “thermal” velocity, $N = M_2/m_H$ is the total number of NM nuclei, and m_H is the molecular mass of hydrogen. Furthermore, we assume an extreme case of $M_1 \sim 0.1 M_\odot$, $M_2 \sim 10.0 M_\odot$. For a typical collapsing molecular cloud, we have $T \sim 150$ K and $\rho_2 \sim 10^8 m_H \text{ cm}^{-3}$, and hence $R_2 = 3.05 \times 10^{16}$ cm is smaller than the Jeans radius. We solve $E(R_2) = 0$ to obtain the maximum DM velocity of DM $v_{1\text{max}} \sim 1.27 \times 10^6 \text{ cm s}^{-1}$. Any $v_1 < v_{1\text{max}}$ would give us a set of solution for R_1 and ρ_1 . However, the most probable DM speed (assuming a Maxwell distribution) is $v_{p1} \sim 10^7 \text{ cm s}^{-1}$. To take the velocity of DM into account, the bounded DM fraction is given by f :

$$f = \frac{\int_0^{u_1} u^2 \exp(-u^2) du}{\int_0^\infty u^2 \exp(-u^2) du}. \quad (\text{A2})$$

Here, $u = v/v_{p1}$, and $u_1 = v_1/v_{p1}$. We take a particular $v_1 = 1.23 \times 10^6 \text{ cm s}^{-1}$, and give two sets of solutions in (R_1, ρ_1) for $E < 0$: $(1.71 \times 10^{18} \text{ cm}, 3860 \text{ GeV/cm}^3)$ and $(6.10 \times 10^{16} \text{ cm}, 8.48 \times 10^7 \text{ GeV/cm}^3)$. The required DM density in the first set of solutions is based on the state-of-the-art simulations, which showed that the DM density at the galactic bulge could be $\sim 3600 \text{ GeV cm}^{-3}$ (Piffi et al. 2014). The required DM density in the other set of solutions is much larger. However, such a value is possible near the galactic center, and values with a similar order of magnitude have been adopted in studying the effect of DM annihilation on main-sequence stars (Moskalenko & Wai 2006; Iocco 2008). In conclusion, our estimations considering the DM velocity dispersions show that it is possible to trap a DM of $0.1 M_\odot$ during the star-forming phase, provided that the molecular cloud is in the vicinity of the galactic center. There might be concern about whether the DM would follow the collapse of the NM to form a composite bound object. We show in the earlier section that a collapsing NM component would eventually induce a collapsing DM component to form a DM-admixed stellar object. And this would, in our case, be a DM-admixed neutron star. Also, the collapse of the DM component happens with a time scale comparable to that of the NM, regardless of its size and mass. By simple scaling relations, we can roughly conclude that the same scenario should also hold for molecular cloud collapse. Therefore, a zero-age main-sequence with an inherent DM admixture should be possible, though a detailed numerical simulation shall be employed to justify our conjecture.

B. DARK MATTER GRAVITATIONAL WAVES FOR RIGIDLY-ROTATING PROGENITORS

In section 3.2.2 we showed the features for DM GWs from differentially-rotating progenitors and proved that they are detectable by the Advanced LIGO, provided that the DM particle mass is 0.3 GeV. Here, we perform a similar analysis

for rigidly-rotating progenitors. In Figure 14 (a), we show the GW spectrograms for rigidly-rotating progenitors. These progenitors are rotating at ~ 0.97 that of the critical velocity and have increasing DM mass fraction ϵ from 0 to 0.2. We observe that the DM GWs can also be captured as continuous low-frequency (< 1000 Hz) signals. In Figure 14 (b), we observe that all peak frequency signals of the DM GWs are detectable by the Advanced LIGO.

REFERENCES

- Abbott, R., et al. 2020, *The Astrophysical Journal*, 896, L44, doi: [10.3847/2041-8213/ab960f](https://doi.org/10.3847/2041-8213/ab960f)
- Abdikamalov, E. B., Ott, C. D., Rezzolla, L., et al. 2010, *Phys. Rev. D*, 81, 044012, doi: [10.1103/PhysRevD.81.044012](https://doi.org/10.1103/PhysRevD.81.044012)
- Aksenov, A. G., & Blinnikov, S. I. 1994, *A&A*, 290, 674
- Arun, K., Gudennavar, S. B., Prasad, A., & Sivaram, C. 2019, *Ap&SS*, 364, 24, doi: [10.1007/s10509-019-3511-6](https://doi.org/10.1007/s10509-019-3511-6)
- Barsotti, L., Fritschel, P., Evans, M., & Gras, S. 2018, LIGO-T1800042-v5, Tech. rep., LIGO
- Bell, N. F., Melatos, A., & Petraki, K. 2013, *Phys. Rev. D*, 87, 123507, doi: [10.1103/PhysRevD.87.123507](https://doi.org/10.1103/PhysRevD.87.123507)
- Bera, P., & Bhattacharya, D. 2016, *Monthly Notices of the Royal Astronomical Society*, 456, 3375, doi: [10.1093/mnras/stv2823](https://doi.org/10.1093/mnras/stv2823)
- Bhat, S. A., & Paul, A. 2020, *European Physical Journal C*, 80, 544, doi: [10.1140/epjc/s10052-020-8072-x](https://doi.org/10.1140/epjc/s10052-020-8072-x)
- Boshkayev, K. 2018, *Astronomy reports*, 62, 847
- Bramante, J., Fukushima, K., & Kumar, J. 2013, *Phys. Rev. D*, 87, 055012, doi: [10.1103/PhysRevD.87.055012](https://doi.org/10.1103/PhysRevD.87.055012)
- Brooks, J., Schwab, J., Bildsten, L., Quataert, E., & Paxton, B. 2017, *The Astrophysical Journal*, 843, 151, doi: [10.3847/1538-4357/aa79a6](https://doi.org/10.3847/1538-4357/aa79a6)
- Casanellas, J., & Lopes, I. 2009, *The Astrophysical Journal*, 705, 135, doi: [10.1088/0004-637x/705/1/135](https://doi.org/10.1088/0004-637x/705/1/135)
- Chan, H.-S., chung Chu, M., Leung, S.-C., & Lin, L.-M. 2021, *The Astrophysical Journal*, 914, 138, doi: [10.3847/1538-4357/abfd32](https://doi.org/10.3847/1538-4357/abfd32)
- Chatterjee, D., Fantina, A. F., Chamel, N., Novak, J., & Oertel, M. 2017, *Monthly Notices of the Royal Astronomical Society*, 469, 95, doi: [10.1093/mnras/stx781](https://doi.org/10.1093/mnras/stx781)
- Clea, S., Kenath, A., Sivaram, C., & Gudennavar, S. 2020, *Physics of the Dark Universe*, 30, 100727, doi: <https://doi.org/10.1016/j.dark.2020.100727>
- Colella, P., & Woodward, P. R. 1984, *Journal of Computational Physics*, 54, 174, doi: [10.1016/0021-9991\(84\)90143-8](https://doi.org/10.1016/0021-9991(84)90143-8)
- Couch, S. M., Graziani, C., & Flocke, N. 2013, *The Astrophysical Journal*, 778, 181, doi: [10.1088/0004-637x/778/2/181](https://doi.org/10.1088/0004-637x/778/2/181)
- Darbha, S., Metzger, B. D., Quataert, E., et al. 2010, *MNRAS*, 409, 846, doi: [10.1111/j.1365-2966.2010.17353.x](https://doi.org/10.1111/j.1365-2966.2010.17353.x)
- Das, H. C., Kumar, A., & Patra, S. K. 2021, *PhRvD*, 104, 063028, doi: [10.1103/PhysRevD.104.063028](https://doi.org/10.1103/PhysRevD.104.063028)
- Dessart, L., Burrows, A., Ott, C. D., et al. 2006, *The Astrophysical Journal*, 644, 1063, doi: [10.1086/503626](https://doi.org/10.1086/503626)
- Eriguchi, Y., & Mueller, E. 1985, *A&A*, 146, 260
- Fink, M., Kromer, M., Hillebrandt, W., et al. 2018, *A&A*, 618, A124, doi: [10.1051/0004-6361/201833475](https://doi.org/10.1051/0004-6361/201833475)
- Finn, L. S., & Evans, C. R. 1990, *ApJ*, 351, 588, doi: [10.1086/168497](https://doi.org/10.1086/168497)
- Flanagan, E. E., & Hughes, S. A. 1998, *Phys. Rev. D*, 57, 4535, doi: [10.1103/PhysRevD.57.4535](https://doi.org/10.1103/PhysRevD.57.4535)
- Franzon, B., & Schramm, S. 2015, *Phys. Rev. D*, 92, 083006, doi: [10.1103/PhysRevD.92.083006](https://doi.org/10.1103/PhysRevD.92.083006)
- Freese, K. 2017, *International Journal of Modern Physics D*, 26, 1730012, doi: [10.1142/S0218271817300129](https://doi.org/10.1142/S0218271817300129)
- Fryer, C. L., & New, K. C. B. 2011, *Living Reviews in Relativity*, 14, 1, doi: [10.12942/lrr-2011-1](https://doi.org/10.12942/lrr-2011-1)
- Gottlieb, S., Ketcheson, D., & Shu, C.-W. 2011, *Strong Stability Preserving Runge-Kutta and Multistep Time Discretizations (WORLD SCIENTIFIC)*, doi: [10.1142/7498](https://doi.org/10.1142/7498)
- Gvaramadze, V. V., Gräfenner, G., Langer, N., et al. 2019, *Nature (London)*, 569, 684
- Hachisu, I. 1986, *ApJS*, 61, 479, doi: [10.1086/191121](https://doi.org/10.1086/191121)
- Iocco, F. 2008, *ApJL*, 677, L1, doi: [10.1086/587959](https://doi.org/10.1086/587959)
- Iorio, L. 2010, *Journal of Cosmology and Astroparticle Physics*, 2010, 046–046, doi: [10.1088/1475-7516/2010/11/046](https://doi.org/10.1088/1475-7516/2010/11/046)
- Kawaler, S. D. 2004, in *Stellar Rotation*, ed. A. Maeder & P. Eenens, Vol. 215, 561
- Langer, N., Yoon, S. C., Petrovic, J., & Heger, A. 2003, *arXiv e-prints, astro*, <https://arxiv.org/abs/astro-ph/0302232>
- Lee, B. K. K., Chu, M.-c., & Lin, L.-M. 2021, *ApJ*, 922, 242, doi: [10.3847/1538-4357/ac2735](https://doi.org/10.3847/1538-4357/ac2735)
- Leung, K.-L., Chu, M.-c., & Lin, L.-M. 2022, *Phys. Rev. D*, 105, 123010, doi: [10.1103/PhysRevD.105.123010](https://doi.org/10.1103/PhysRevD.105.123010)
- Leung, S.-C., & Nomoto, K. 2019, *PASA*, 36, e006, doi: [10.1017/pasa.2018.49](https://doi.org/10.1017/pasa.2018.49)
- Leung, S.-C., Nomoto, K., & Suzuki, T. 2020, *The Astrophysical Journal*, 889, 34, doi: [10.3847/1538-4357/ab5d2f](https://doi.org/10.3847/1538-4357/ab5d2f)

- Leung, S.-C., Zha, S., Chu, M.-C., Lin, L.-M., & Nomoto, K. 2019, *The Astrophysical Journal*, 884, 9, doi: [10.3847/1538-4357/ab3b5e](https://doi.org/10.3847/1538-4357/ab3b5e)
- Liebendorfer, M. 2005, *The Astrophysical Journal*, 633, 1042–1051, doi: [10.1086/466517](https://doi.org/10.1086/466517)
- Liu, D., & Wang, B. 2020, *Monthly Notices of the Royal Astronomical Society*, 494, 3422, doi: [10.1093/mnras/staa963](https://doi.org/10.1093/mnras/staa963)
- Lopes, J., & Lopes, I. 2019, *The Astrophysical Journal*, 879, 50, doi: [10.3847/1538-4357/ab2392](https://doi.org/10.3847/1538-4357/ab2392)
- Margalit, B., Berger, E., & Metzger, B. D. 2019, *ApJ*, 886, 110, doi: [10.3847/1538-4357/ab4c31](https://doi.org/10.3847/1538-4357/ab4c31)
- Mignone, A. 2014, *Journal of Computational Physics*, 270, doi: [10.1016/j.jcp.2014.04.001](https://doi.org/10.1016/j.jcp.2014.04.001)
- Moenchmeyer, R., Schaefer, G., Mueller, E., & Kates, R. E. 1991, *A&A*, 246, 417
- Moriya, T. J. 2016, *ApJL*, 830, L38, doi: [10.3847/2041-8205/830/2/L38](https://doi.org/10.3847/2041-8205/830/2/L38)
- Moskalenko, I. V., & Wai, L. L. 2006, arXiv e-prints, astro. <https://arxiv.org/abs/astro-ph/0608535>
- Müller, B., Dimmelmeier, H., & Müller, E. 2008, *A&A*, 489, 301, doi: [10.1051/0004-6361:200809609](https://doi.org/10.1051/0004-6361:200809609)
- Murphy, J. W., Ott, C. D., & Burrows, A. 2009, *ApJ*, 707, 1173, doi: [10.1088/0004-637X/707/2/1173](https://doi.org/10.1088/0004-637X/707/2/1173)
- Narain, G., Schaffner-Bielich, J., & Mishustin, I. N. 2006, *Phys. Rev. D*, 74, 063003, doi: [10.1103/PhysRevD.74.063003](https://doi.org/10.1103/PhysRevD.74.063003)
- Nitz, A., Harry, I., Brown, D., et al. 2022, gwastro/pycbc: v2.0.5 release of PyCBC, v2.0.5, Zenodo, doi: [10.5281/zenodo.6912865](https://doi.org/10.5281/zenodo.6912865)
- Nomoto, K., & Kondo, Y. 1991, *ApJL*, 367, L19, doi: [10.1086/185922](https://doi.org/10.1086/185922)
- Ott, C. D. 2009, *Classical and Quantum Gravity*, 26, 063001, doi: [10.1088/0264-9381/26/6/063001](https://doi.org/10.1088/0264-9381/26/6/063001)
- Ott, C. D., Burrows, A., Livne, E., & Walder, R. 2004, *ApJ*, 600, 834, doi: [10.1086/379822](https://doi.org/10.1086/379822)
- Ott, C. D., Ou, S., Tohline, J. E., & Burrows, A. 2005, *ApJL*, 625, L119, doi: [10.1086/431305](https://doi.org/10.1086/431305)
- Peter, A. H. G. 2012, arXiv e-prints, arXiv:1201.3942. <https://arxiv.org/abs/1201.3942>
- Pfannes, J. M. M., Niemeyer, J. C., & Schmidt, W. 2010, *A&A*, 509, A75, doi: [10.1051/0004-6361/200912033](https://doi.org/10.1051/0004-6361/200912033)
- Piffl, T., Binney, J., McMillan, P. J., et al. 2014, *MNRAS*, 445, 3133, doi: [10.1093/mnras/stu1948](https://doi.org/10.1093/mnras/stu1948)
- Pshirkov, M. S., Dodin, A. V., Belinski, A. A., et al. 2020, *Monthly Notices of the Royal Astronomical Society: Letters*, 499, L21, doi: [10.1093/mnrasl/slaa149](https://doi.org/10.1093/mnrasl/slaa149)
- Raen, T. J., Martínez-Rodríguez, H., Hurst, T. J., et al. 2021, *Monthly Notices of the Royal Astronomical Society*, 503, 5611, doi: [10.1093/mnras/stab865](https://doi.org/10.1093/mnras/stab865)
- Reisswig, C., & Pollney, D. 2011, *Classical and Quantum Gravity*, 28, 195015, doi: [10.1088/0264-9381/28/19/195015](https://doi.org/10.1088/0264-9381/28/19/195015)
- Richers, S., Ott, C. D., Abdikamalov, E., O’Connor, E., & Sullivan, C. 2017, *PhRvD*, 95, 063019, doi: [10.1103/PhysRevD.95.063019](https://doi.org/10.1103/PhysRevD.95.063019)
- Ruiter, A. J., Ferrario, L., Belczynski, K., et al. 2019, *Monthly Notices of the Royal Astronomical Society*, 484, 698, doi: [10.1093/mnras/stz001](https://doi.org/10.1093/mnras/stz001)
- Shen, H., Toki, H., Oyamatsu, K., & Sumiyoshi, K. 1998, *Progress of Theoretical Physics*, 100, 1013, doi: [10.1143/PTP.100.1013](https://doi.org/10.1143/PTP.100.1013)
- Skinner, M. A., Burrows, A., & Dolence, J. C. 2016, *ApJ*, 831, 81, doi: [10.3847/0004-637X/831/1/81](https://doi.org/10.3847/0004-637X/831/1/81)
- Spruit, H. C. 1998, *A&A*, 333, 603. <https://arxiv.org/abs/astro-ph/9802141>
- Sulistiyowati, Wulandari, H., Dermawan, B., Arifyanto, M. I., & Ibrahim, I. 2014, in *American Institute of Physics Conference Series*, Vol. 1589, 4th International Conference on Mathematics and Natural Sciences (ICMNS 2012): Science for Health, Food and Sustainable Energy, 33–36, doi: [10.1063/1.4868744](https://doi.org/10.1063/1.4868744)
- Toro, E. 2009, *Riemann Solvers and Numerical Methods for Fluid Dynamics: A Practical Introduction*, doi: [10.1007/b79761](https://doi.org/10.1007/b79761)
- Wang, B. 2018, *Monthly Notices of the Royal Astronomical Society*, 481, 439, doi: [10.1093/mnras/sty2278](https://doi.org/10.1093/mnras/sty2278)
- Wang, B., Justham, S., Liu, Z.-W., et al. 2014, *Monthly Notices of the Royal Astronomical Society*, 445, 2340, doi: [10.1093/mnras/stu1891](https://doi.org/10.1093/mnras/stu1891)
- Wang, B., & Liu, D. 2020, *Research in Astronomy and Astrophysics*, 20, 135, doi: [10.1088/1674-4527/20/9/135](https://doi.org/10.1088/1674-4527/20/9/135)
- Wang, B., Liu, D., & Chen, H. 2022, *MNRAS*, 510, 6011, doi: [10.1093/mnras/stac114](https://doi.org/10.1093/mnras/stac114)
- Wu, C.-Y., & Wang, B. 2018, *Research in Astronomy and Astrophysics*, 18, 036, doi: [10.1088/1674-4527/18/3/36](https://doi.org/10.1088/1674-4527/18/3/36)
- Yoon, S.-C., & Langer, N. 2004, *Astronomy & Astrophysics*, 419, 623–644, doi: [10.1051/0004-6361:20035822](https://doi.org/10.1051/0004-6361:20035822)
- Yoon, S.-C., & Langer, N. 2005, *A&A*, 435, 967, doi: [10.1051/0004-6361:20042542](https://doi.org/10.1051/0004-6361:20042542)
- Yoshida, S. 2019, *Monthly Notices of the Royal Astronomical Society*, 486, 2982–2994, doi: [10.1093/mnras/stz1030](https://doi.org/10.1093/mnras/stz1030)
- Zha, S., Chu, M.-C., Leung, S.-C., & Lin, L.-M. 2019a, *The Astrophysical Journal*, 883, 13, doi: [10.3847/1538-4357/ab3640](https://doi.org/10.3847/1538-4357/ab3640)
- Zha, S., Leung, S.-C., Suzuki, T., & Nomoto, K. 2019b, *The Astrophysical Journal*, 886, 22, doi: [10.3847/1538-4357/ab4b4b](https://doi.org/10.3847/1538-4357/ab4b4b)

781 Zha, S., O'Connor, E. P., Chu, M.-c., Lin, L.-M., & Couch,
782 S. M. 2020, PhRvL, 125, 051102,
783 doi: [10.1103/PhysRevLett.125.051102](https://doi.org/10.1103/PhysRevLett.125.051102)

784 Zingale, M., Almgren, A. S., Barrios Sazo, M., et al. 2020,
785 in Journal of Physics Conference Series, Vol. 1623,
786 Journal of Physics Conference Series, 012021,
787 doi: [10.1088/1742-6596/1623/1/012021](https://doi.org/10.1088/1742-6596/1623/1/012021)